

Two Bogoliubov quasiparticles entangled by a spin

Juan Carlos Estrada Saldaña^{1,*}, Alexandros Vekris^{1,2}, Luka Pavešič^{3,4},

Rok Žitko^{3,4}, Kasper Grove-Rasmussen¹, and Jesper Nygård¹

¹Center for Quantum Devices, Niels Bohr Institute,
University of Copenhagen, 2100 Copenhagen, Denmark

²Sino-Danish College (SDC), University of Chinese Academy of Sciences

³Jožef Stefan Institute, Jamova 39, SI-1000 Ljubljana, Slovenia and

⁴Faculty of Mathematics and Physics, University of Ljubljana, Jadranska 19, SI-1000 Ljubljana, Slovenia

Condensed matter is composed of a small set of identical units which nevertheless show an immense range of behaviour. Recently, an array of atoms was used to generate long-range spin entanglement, a property of topological matter¹. A different approach is to employ the macroscopic coherence of superconductors^{2,3}. However, the presence of a single localized spin is naively expected to disrupt any form of long-range spin entanglement by binding to a quasiparticle from the superconductor to form a localized singlet bound state^{4,5}. Here we demonstrate that it is possible to attach a second quasiparticle to the spin, overscreening it into a doublet state carrying triplet correlations between the quasiparticles over a micrometer distance. To demonstrate this effect, which is strongest for symmetric bindings, we couple with equal strength the spin of a quantum dot to two superconducting islands in which the Coulomb repulsion overcomes Cooper pairing. We show that the doublet state is stabilized by the Coulomb repulsion and destabilized by the singlet binding. We predict that this state will carry triplet correlations for an alternating chain of any odd number of quantum dots and superconducting islands, opening an alternative route to controllable long-range entanglement in the solid state.

The alternating superconducting island (SI)-quantum dot (QD) chain is schematized in Fig. 1a. The SIs have equal Coulomb repulsion E_c and superconducting energy gap Δ , while the QDs have equal Coulomb repulsion U . A Bogoliubov quasiparticle occupies each SI, which is facilitated for $E_c > \Delta$. The Yu-Shiba-Rusinov (YSR) interaction binds each quasiparticle to an antiparallel spin in the adjacent QD^{4,5}. When the YSR binding energy E_B is equal among all SI-QD pairs, the ground state (GS) of the whole system becomes a doublet with long-range triplet correlations between the end spins. As shown in Fig. 1b, the correlations decrease with the chain length, but are recovered by increasing E_c/Δ which stabilizes the local moment (LM) in the SIs. The doublet state is self-similar for chains of any odd number of elements as long as E_c/Δ is sizable (see Extended Data Fig. 1). Therefore, a three-element chain (box in Fig. 1a) is representative of the longer chain, and it is the unit investigated here.

Our chain device is shown in Fig. 1c. An InAs semi-

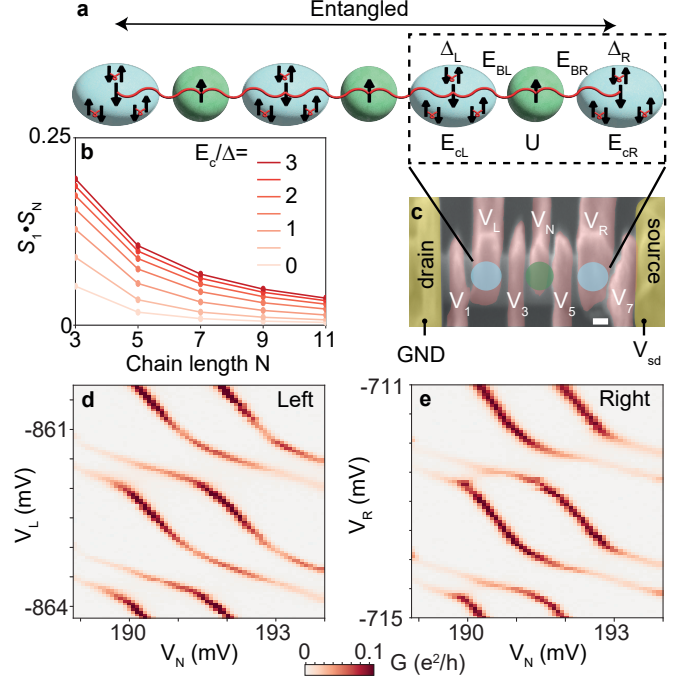


FIG. 1. Chain of Bogoliubov quasiparticles entangled by electron spins. **a** Alternating superconducting island-quantum dot chain. Each SI has a Coulomb-blockaded quasiparticle and each QD has a Coulomb-blockaded spin. In this arrangement, the Yu-Shiba-Rusinov interaction binds antiferromagnetically neighboring local moments (LMs) of the chain. For equal bindings and equal parameters among the QDs and the SIs, each QD spin is overscreened by its two QP neighbors, carrying long-range triplet correlations between every second element in an extended doublet ground state. **b** Calculation of correlations between the spins at the ends of the chain versus chain length for a range of Coulomb repulsions E_c . **c** Device used to realize a three-element chain consisting of a QD coupled to two SIs. Scale bar is 100 nm. **d,e** Zero-bias conductance G versus V_N , and **(d)** V_L or **(e)** V_R . The resemblance in the conductance patterns in the two diagrams reflects the high degree of left-right symmetry of the device parameters in this gate configuration, with differences in E_c/Δ and binding E_B being 8% and 14%.

conductor nanowire hosts a gate-defined QD whose occupation is tuned with top gate voltage V_N . The binding energies E_{BL}, E_{BR} to two Al SIs are tuned with top gate voltages V_3 and V_5 . The occupations of the SIs are

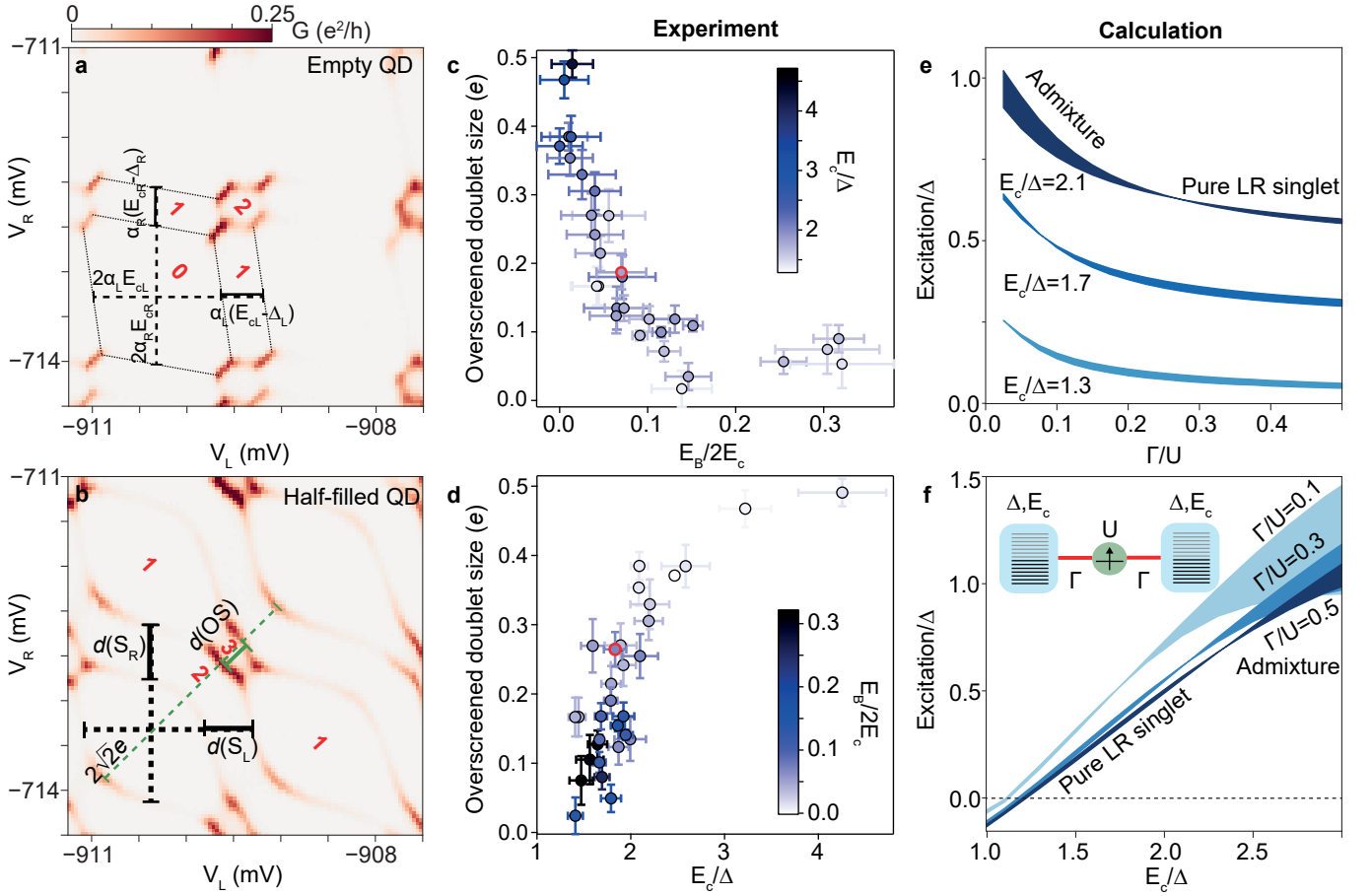


FIG. 2. **Binding two quasiparticles to a spin.** **a,b** Zero-bias G stability diagram versus V_L and V_R , for **a** empty QD, **b** QD filled with one LM. The number of LMs in the full device is indicated in red numbers. Solid bars in **(a)** normalized by the dashed bars provide $E_{cL,cR}/\Delta$ independent of the gate-to-energy conversion factors $\alpha_{L,R}$. When normalized by the dashed bars, the solid horizontal and vertical bars in **(b)** minus those in **(a)** provide $E_B/2E_c$. The diagonal solid bar of length $d(OS)$ in **(b)** measures size of the overscreened doublet when it is the GS. The diagonal dashed bar measures the gate voltage needed to add two electrons in each SI, and we use it as a normalization factor for the OS size. **c** Normalized OS doublet size in 26 QD shells, against $E_B/2E_c$. $E_c/\Delta = 1.3 - 4.2$, given by the colorscale. Left-right differences in E_B and E_c/Δ are 0-30%. $U/\Delta = 2 - 4$ measured from Coulomb diamonds spectroscopy. **d** Data from **(c)** plotted against E_c/Δ . $E_B/2E_c = 0 - 0.32$, given by the colorscale. The red circle indicates the data point extracted from **(a,b)**. Error bars are based on the full width at half-maximum of the conductance lines used in the extraction of the data. **e** Calculated doublet \rightarrow singlet excitation energy versus Γ/U in the center of the 3 LM sector for different E_c/Δ . **f** Calculated doublet \rightarrow singlet excitation energy versus E_c/Δ for different Γ/U . Inset. Cartoon of the model used for the calculations. Bands in **(e,f)** indicate the range $U/\Delta = 2 - 4$ used in the calculations.

individually varied with top gate voltages V_L and V_R . E_{cL}/Δ_L and E_{cR}/Δ_R are individually tuned by V_L and V_R and set to $E_{cL} > \Delta_L$ and $E_{cR} > \Delta_R$, which lets a quasiparticle occupy each SI at the appropriate gate settings. Standard lock-in techniques are used to obtain the differential conductance G , which when peaked reflects excitations between chain states.

We set our device to approximately left-right symmetric E_c/Δ and E_B . The symmetry is directly evaluated from pairs of zero-bias G diagrams, of which an example is shown in Figs. 1d,e. At zero-bias, lines in the colormaps represent singlet \leftrightarrow doublet GS crossings, and the size of the regions bounded by the lines reflects the stability of a given GS. This size depends not only on the GS en-

ergy, but also on the energy of the GS at the neighboring regions. Besides on high tunability, the symmetry relies on designing the SIs to be nominally identical by crystal growth and lithography, an advantage over gate-defined QD chains⁶.

The states of the SI-QD-SI chain depend on the LM distribution and are sketched in Extended Data Fig. 2. In the absence of LMs, the GS is a trivial singlet formed by Cooper pair states. Adding a LM into one element of the chain changes the GS into a trivial doublet. When the SIs each host a LM, they form an inter-SI singlet. Two LMs can also be distributed between the QD and the SIs, leading to a left-right (LR) singlet formed by the even superposition of the two possible YSR singlets. An

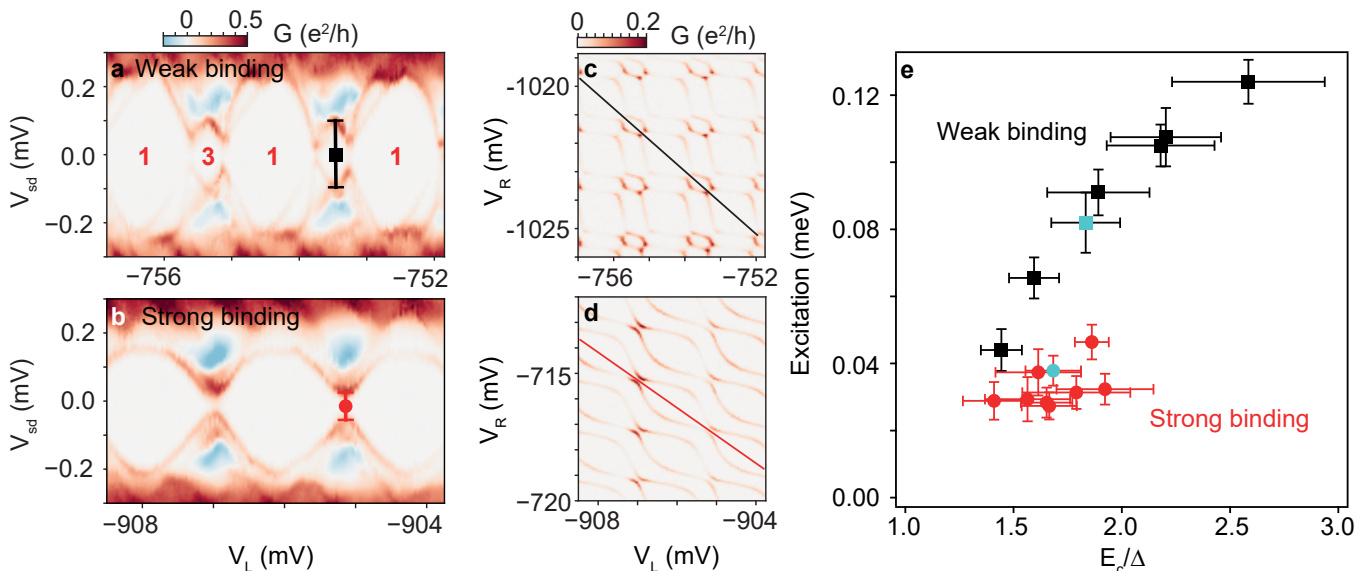


FIG. 3. **Coulomb-stabilized excitations.** **a,b** Examples of bias spectra for **(a)** weak and **(b)** strong E_B . **c,d** Zero-bias G stability diagrams with 1 LM fixed in the QD. Solid lines indicate the V_L , V_R trajectories in **(a)**, **(b)**. In these trajectories, the number of LMs in the SIs is varied between 2 and 0 in alternation. Red numbers **(a)**, **(b)** indicate the total number of LMs in the GS. **e** Doublet \rightarrow singlet excitation energies in the middle of the OS GS sector versus approximately symmetric E_c/Δ , with left-right differences being less than 25%. Black squares (red circles) correspond to weak (strong) binding. To avoid zero-bias offset issues, the excitation energies are measured as the average of the sum of the addition and removal energies. The sum is given by vertical bars in the examples in **(a)**, **(b)**. Blue symbols are the excitation energy values extracted from these examples. Error bars are based on the full width at half-maximum of the conductance lines used in the extraction of the data. The weak-binding data is expected to fully saturate at an excitation energy equal to $U/2 = 0.15$ meV, where U is measured from Coulomb-diamonds spectroscopy.

additional LM may be attached to the LR singlet, forming an overscreened (OS) doublet where the QD spin is maximally entangled with the spins of the SIs. Additionally, there is an excited decoupled (i.e., disentangled) doublet which can become the GS for $E_c < \Delta$. For details, see Supplementary Information.

The gate voltage controls the number and distribution of LMs, leading to a competition of the states for being the GS at a given gate voltage. The OS doublet is most stable in the 3 LM sector. We examine how its size is affected by the variation of device parameters. Figs. 2a,b show examples of zero-bias G stability diagrams versus V_L , V_R when the QD is empty (a) and when it is filled with one LM (b) to illustrate how the OS doublet size and the parameters E_c/Δ and E_B are gauged. The parameters can be reliably extracted in this way due to the periodicity of the diagrams (period given by dashed lines).

We apply these methods to the diagrams of 26 QD shells and compile our results of the overscreened doublet size against the binding energy and the Coulomb repulsion in Figs. 2c,d. In QD-SI dimers, the binding interaction always stabilizes the screened state, with its size reaching $2e$ for strong binding^{4,5}. Figure 2c shows that the opposite occurs for the OS state in our device, with the OS size decreasing sharply with the binding strength. Also in dimers, large E_c/Δ stabilizes the screened state

by forming a LM in the SI, leading to its size in the GS stability diagram converging to $1e$ independently of the binding strength⁴, where $1e$ is the gate voltage needed to add a single quasiparticle in the $E_c/\Delta \rightarrow \infty$ limit. In our device, as shown in Fig. 2d, the OS size grows linearly at first and then goes sub-linearly until $0.5e$. Strong binding is reached by setting the gate voltages more positive, which prevents large E_c/Δ , thus clustering the data points in two portions. These clusters appear at small E_c/Δ for strong binding and at large E_c/Δ for weak binding, as shown by the colorscales in Figs. 2c,d.

To interpret the data, we use calculations of the excitation energy between the OS GS and the lowest singlet excited state in Figs. 2e,f obtained with the Hamiltonian schematized in the inset of Fig. 2f and solved by the density matrix renormalization group (DMRG)^{7,8}. Γ is the hybridization between the SI and the QD that controls E_B . In Fig. 2c, the fast decrease at low Γ/U and subsequent saturation at large Γ/U for different $E_c/\Delta > 1$ is a consequence of the change of the singlet nature from an admixture of LR and inter-SI to pure LR. The large admixture comes from $U/2 \sim \Delta \sim E_c$; large U would make the inter-SI singlet irrelevant. Importantly, the saturation indicates that both the OS and singlet states are gaining the same energy with an increase in binding, thus identifying the singlet as LR and the doublet as OS. When pure, the states are each maximally entangled. In

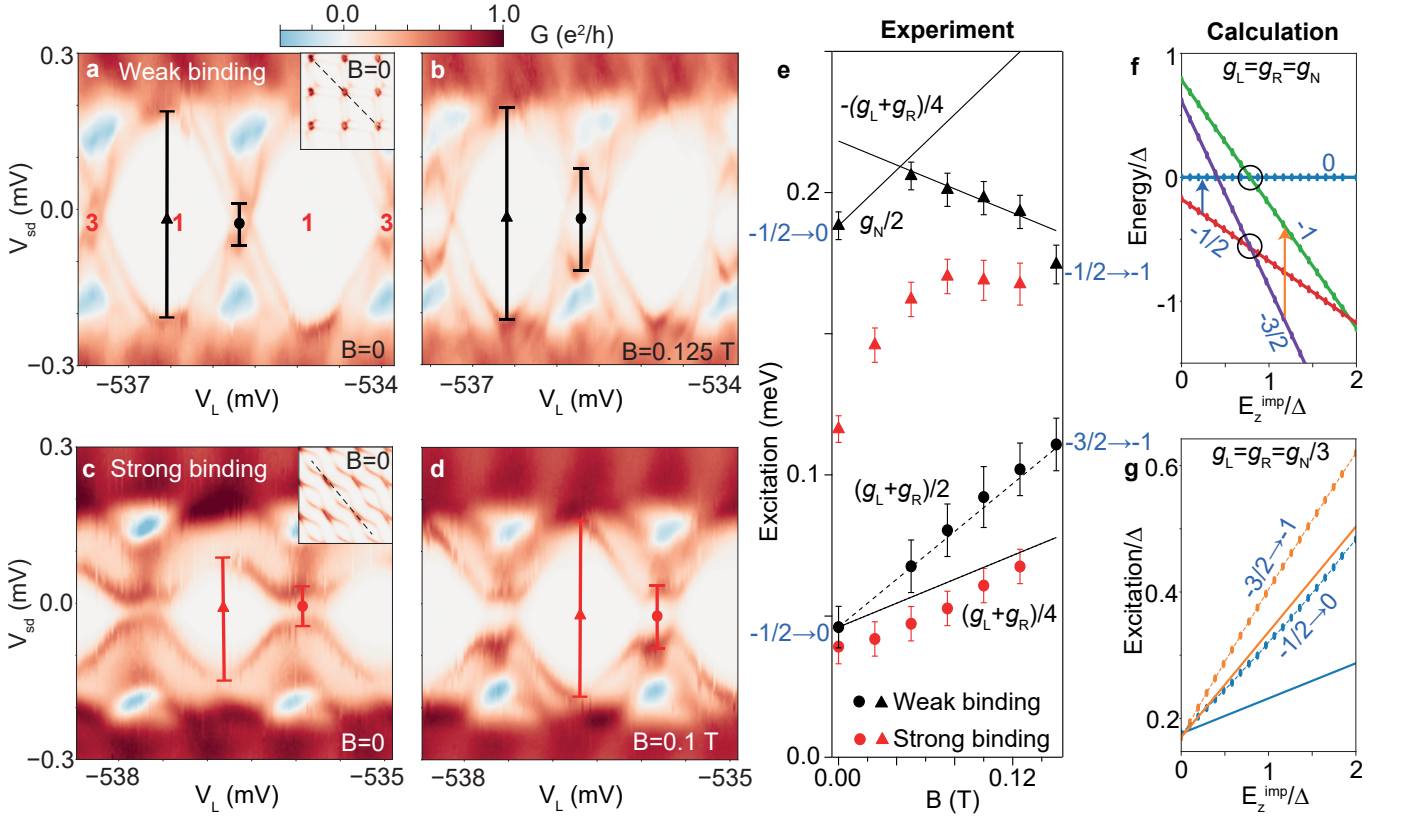


FIG. 4. **Polarizing two bound Bogoliubov quasiparticles with a magnetic field.** **a-d** Bias spectra for approximately left-right symmetric parameters, with **(a,b)** $E_B/2E_c = 0.04$ (weak binding), $E_c/\Delta = 1.45$ and **(c,d)** $E_B/2E_c = 0.32$ (strong binding), $E_c/\Delta = 1.65$, recorded at different B indicated on each plot. The gate sweep, indicated by a dashed line in the inset stability diagrams in **(a,c)** for $B = 0$, alternates the total number of LMs between 1 and 3, while keeping a LM fixed in the QD. At $B = 0$, the GS is a doublet and the first excited state a singlet. These states are overran by higher-spin states at larger B . **e** B dependence of excitation energy for weak (black symbols) and strong (red symbols) binding. Circles indicate measurements taken with 3 LMs in the device, and triangles those taken with only 1 LM. To avoid zero-bias offset issues, the excitations are measured as the average of the sum of the addition and removal excitations, where the sum is given by bars in **(a-d)**. Solid lines indicate slopes expected in a calculation which assumes pure states only (PSO) written in terms of the experimentally obtained g -factors in the weak-binding case. Blue numbers denote the spin S_z of the states involved in the excitations for $B = 0$ and largest B . For simplicity, μ_B has been dropped. The measured slope is twice as big as the expectation for the $-3/2 \rightarrow -1$ excitation. A dashed line with twice the slope has been drawn to indicate this. **(f)** Calculation of the spectrum versus the Zeeman energy of the QD, E_z^{imp} , for equal g -factors and 3 LMs. The full DMRG calculation (dots) agrees with PSO (lines). Circles indicate the crossing of the $-1/2$ and $-3/2$ states and the 0 and -1 states. Excitations relevant for the experiment are given by arrows. **(g)** Calculation of excitations for uneven g -factors as in the experiment. PSO (lines) underestimates the result of the full DMRG calculation (dots). $U/\Delta = 4$ and $\Gamma/U = 0.3$.

the experiment (Fig. 2c), a saturation of the OS size can be seen for strong binding, indicative of the purity of the LR and OS states.

Pure LR and OS states can also be deduced from the linear dependence of the excitation energy on E_c/Δ seen in Fig. 2f for large Γ/U . The OS size versus E_c/Δ in Fig. 2d displays a linear trend for strong binding, consistent with pure LR and OS states. For small Γ/U , the larger energy of the admixture singlet produces a steeper dependence of the excitation energy on E_c/Δ (Fig. 2f), with a saturation at $U/2\Delta$ due to the singlet gaining strong inter-SI nature. The admixture explains the sub-linear growth of the OS size ending at $0.5e$ observed in the experiment in Fig. 2d.

When $E_c/\Delta < 1$, the GS changes to the trivial doublet for weak binding, small E_c/Δ , and to the LR singlet for strong binding, $E_c/\Delta \sim 1$. Data around the transition $E_c/\Delta = 1$ is shown in Extended Data Fig. 3.

To enable a direct comparison with the calculations in Fig. 2f, we measure the excitation energy. The excitation spectrum can be read from peaks in $G(V_{sd})$, where V_{sd} is the source-drain bias voltage across the device. Figs. 3a,b show examples of the spectrum for weak and strong binding. They are obtained by sweeping V_L , V_R in a trajectory indicated in the stability diagrams in Figs. 3c,d which maintains the doublet as the GS. We focus on the peaks at lowest V_{sd} . They are qualitatively consistent with the output of the DMRG calcu-

lation shown in Extended Data Fig. 4. For weak binding, the spectrum shows diamond-like features with the small diamonds defined by OS \rightarrow LR excitations. Strong binding mixes states of the same total charge, transforming the small diamonds into avoided crossings. Fig. 3e compiles OS \rightarrow LR excitations in different QD shells versus E_c/Δ . As before, the data clusters into weak (black squares) and strong (red circles) binding portions, with the latter displaying small E_c/Δ . The data is consistent with the calculations in Fig. 2f and with the shape of the curves in Fig. 2d.

An external magnetic field (B) polarizes the LMs in the chain, leading to changes in the spectrum as LR triplet and quadruplet states of spin $S_z = 1$ and $3/2$ join the OS doublet and the LR singlet of spin $S_z = 1/2$ and 0 at low energy. Figs. 4a-d show spectra for weak and strong binding at two B values to illustrate how excitation energies are extracted in the 1 LM and 3 LM sectors. In Fig. 4e, we show the detailed B dependence of the excitation energy for 1 LM (triangles) and 3 LMs (circles) for the two binding cases. We first focus on the weak binding case (black symbols). Whereas the slope in the 3 LM case is largely constant, it becomes negative in the 1 LM case. We compare our results to estimations assuming states which do not mix at larger B (pure-states only, PSO). Solid bars show the Zeeman shift estimations from the model using the device g -factors. These g -factors, measured by loading a single LM in the relevant device component, are $g_L = 8.7$, $g_N = 17$, $g_R = 5.9$ for the weak-binding dataset, and $g_L = 8.8$, $g_N = 20$, $g_R = 5.7$ for the strong-binding one, where L,N,R stand for left SI, QD, and right SI. Model and data agree in the 1 LM case, with the change of slope interpreted as the triplet replacing the singlet as the first excited state.

However, a quantitative disagreement occurs in the 3 LM case, which derives from the inadequacy of the model for uneven g -factors. Fig. 4f compares the PSO estimation (lines) for the Zeeman evolution of the states with the full DMRG calculation (dots) for equal g -factors for 3 LMs. The agreement is perfect in this case. The calculation also shows that the triplet-singlet crossing is a reliable indicator for the quadruplet-doublet crossing, as they occur at approximately the same B . Uneven g -factors, as shown in Fig. 4g, produce an enhancement of the DMRG estimation of the excitation energy of the two relevant excitations, doublet \rightarrow singlet, and quadruplet \rightarrow triplet, with respect to the PSO estimate (there is no such enhancement in the 1 LM sector). The slopes in Fig. 4e in the 3 LM sectors are consistent with the DMRG estimation of the quadruplet \rightarrow triplet excitation in the weak binding case, indicating that DMRG is more reliable for uneven g -factors. For strong binding, the transition from a doublet \rightarrow singlet excitation to a quadruplet \rightarrow triplet excitation is pushed up to larger B due to larger singlet-triplet splitting, seen as a change of slope at $B = 0.1$ T in Fig. 4e. Additional data is shown in Extended Data Figs. 5 and 6.

In our odd chain, triplet correlations are brought to

the micrometer scale by setting $E_c/\Delta > 1$, in contrast to the nanometer scale of YSR chains of magnetic adatoms on $E_c = 0$ superconducting substrates⁹. Even chains of QD-SI singlet dimers should instead lead to long-range singlet correlations between the end unpaired elements¹⁰, not limited by the superconducting coherence length in contrast to Cooper-pair splitters^{2,3}.

A longer odd chain can be used to demonstrate the self-similar state of the Wilson-chain vision of the two-channel Kondo model¹¹, where the central extended doublet is recursively overscreened by the ending SIs (Figs. 1a,b). The length dependence of the correlations can be investigated by unloading LMs from the elements of the long chain, effectively shortening its length. Possible limitations in obtaining longer chains can be tested in an inverted QD-SI-QD chain, as discussed in Extended Data Fig. 8.

The chain can be mapped to other models by setting its parameters to different limits. For example, for $\Delta = 0$ it maps to the Hubbard chain (triple QD for 3 sites) and, for weak hopping, to the Heisenberg chain. For $E_{BL} \neq E_{BR}$, it realizes the interacting Su-Schrieffer-Heeger model¹², and for $E_c = 0$, $\Delta = 0$ it simulates the Kondo necklace¹³. Extension to two-dimensional lattices is possible by using nanowire networks¹⁴, enabling the pursuit of topological spin liquids¹.

METHODS

Device fabrication. An 120-nm wide InAs nanowire with a 7-nm in-situ grown epitaxial Al shell covering three of its facets was deposited with a micromanipulator on a Si/SiO₂ substrate used as a backgate. The device was defined by a series of electron-beam lithography steps. The Al was patterned into two ≈ 300 -nm long islands by Transene-D etching. The nanowire was contacted by Ti/Au (5/200 nm) leads following a gentle argon milling to remove the nanowire native oxide. A 5-nm thick layer of HfO₂ was deposited over the device to insulate it from seven Ti/Au top gates deposited thereafter. Gates 1 and 7 were respectively short-circuited to gates V_L and V_R .

Measurements. All measurements were performed in an Oxford Triton dilution refrigerator at 30 mK. Higher temperature broadens the G features and erases the even-odd parity alternation of the SIs as expected (see Extended Data Fig. 1). G was measured by biasing the source with a lock-in voltage of $5 \mu\text{V}$ at a frequency 84.29 Hz on top of V_{sd} , and recording the lock-in current at the grounded drain. Zero-bias G was measured at $-18 \mu\text{V}$ to account for an offset in the current amplifier. B was aligned with the nanowire axis to maximize the critical field, B_c . B_c was estimated at > 1.5 T. A single QD was achieved by setting V_3, V_5 to negative values. To achieve left-right symmetry, QD shells with approximately left-right symmetric binding energy were further fine-tuned with V_L and V_R until $E_{cL}/\Delta_L \approx E_{cR}/\Delta_R$. To achieve

the electron-hole symmetric filling of the QD in Figs. 2-4, V_N was fine-tuned until the bottom left and top right parts of the stability diagram were symmetric. Tuning of E_{cL}/Δ_L and E_{cR}/Δ_R was achieved by using two auxiliary QDs, one each to the left and right of the left and right SIs. $E_{cL,R}$ was reduced when these QDs were put in resonance with the drain and source leads. Though in reality a five element QD-SI-QD-SI-QD chain, the device behaved as a shorter SI-QD-SI chain as intended with the outer QDs set in cotunnelling. We speculate that this was due to low tunnel couplings between the auxiliary QDs and the SIs, and/or due to the auxiliary QDs having even occupation.

Asymmetry. Left-right binding asymmetry precludes the inter-island (super-exchange) tunnelling of quasiparticles. Experimentally, this is observed as a weaker reduction of $d(\text{OS})/\sqrt{d(S_L)^2 + d(S_R)^2}$ when one of the binding energies is asymmetrically increased (in comparison to Fig. 3c). A left-right asymmetric increase of E_{cL}/Δ_L , E_{cR}/Δ_R produces a similar stabilization of the doublet domain as for the symmetric E_c/Δ case in Fig. 3d. However, the stabilization is asymmetric in the V_L , V_R gate space, with the largest E_c/Δ enlarging the doublet domain in the corresponding island gate direction in the stability diagram.

Model and calculations. For calculations in Fig. 2e,f, we describe the QD as a single non-degenerate impurity level, as in the single-impurity Anderson model. The SIs are described by the Richardson model, as two sets of equidistant energy levels that represent time-reversal-conjugate pairs in the momentum/orbital space. These are coupled all-to-all by the pairing interaction. This step beyond the BCS mean-field approximation allows for particle number conservation and is required to accurately describe even-odd occupancy effects of the SI with large charging energy E_c . The QD is coupled to all levels of both SIs with the hybridisation terms. The Hamiltonian is

$$H = H_{\text{QD}} + \sum_{\beta=L,R} (H_{\text{SC}}^{(\beta)} + H_{\text{hyb}}^{(\beta)}), \quad (1)$$

where

$$\begin{aligned} H_{\text{QD}} &= \varepsilon_{\text{QD}} \hat{n}_{\text{QD}} + U \hat{n}_{\text{QD},\uparrow} \hat{n}_{\text{QD},\downarrow} + E_{Z,\text{QD}} \hat{S}_z, \\ &= \frac{U}{2} (\hat{n}_{\text{QD}} - \nu)^2 + E_{Z,\text{QD}} \hat{S}_z + \text{const.}, \\ H_{\text{SC}}^{(\beta)} &= \sum_{i,\sigma} \varepsilon_i c_{i,\sigma,\beta}^\dagger c_{i,\sigma,\beta} - \alpha_\beta d \sum_{i,j} c_{i,\uparrow,\beta}^\dagger c_{i,\downarrow,\beta}^\dagger c_{j,\downarrow,\beta} c_{j,\uparrow,\beta} \\ &\quad + E_c^{(\beta)} (\hat{n}_{\text{SC}}^{(\beta)} - n_0^{(\beta)})^2, \\ H_{\text{hyb}}^{(\beta)} &= (v_\beta/\sqrt{N}) \sum_{i,\sigma} (c_{i,\sigma,\beta}^\dagger d_\sigma + d_\sigma^\dagger c_{i,\sigma,\beta}) \\ &\quad + V_\beta (\hat{n}_{\text{QD}} - \nu) (\hat{n}_{\text{SC}}^{(\beta)} - n_0^{(\beta)}). \end{aligned}$$

Here ε_{QD} is the energy level and U the electron-electron repulsion on the QD. The QD term can be rewritten in terms of $\nu = 1/2 - \varepsilon_{\text{QD}}/U$, the QD level in units of electron number. d_σ and $c_{i,\beta,\sigma}$ are the annihilation operators corresponding to the QD and the two SIs labeled by $\beta = L, R$ (left and right). The spin index is $\sigma = \uparrow, \downarrow$. The N SI energy levels ε_i are spaced by a constant separation $d = 2D/N$, where $2D$ is the bandwidth. The levels are coupled all-to-all by a pairing interaction with strength α . The number operators are $\hat{n}_{\text{QD}} = \sum_\sigma d_\sigma^\dagger d_\sigma$ for the QD, and $\hat{n}_{\text{SC}}^{(\beta)} = \sum_{i=1,\sigma}^N c_{i,\sigma,\beta}^\dagger c_{i,\sigma,\beta}$ for each SI. $E_c^{(\beta)}$ are the charging energies, with $n_0^{(\beta)}$ the optimal occupation of the SI in units of electron charge. The SIs are coupled to the QD with the hybridisation strengths $\Gamma_\beta = \pi \rho v_\beta^2$, where $\rho = 1/2D$ is the normal-state density of states in each bath. The V_β terms describe the capacitive coupling between the QD and SI. We take $D = 1$ as the unit of energy.

The results were obtained for $N = 100$ levels in each superconductor and we set $\alpha = 0.4$, which determines the superconducting gap in the absence of the QD, $\Delta = 0.16$. This value is chosen so that an appropriate number of levels is engaged in the pairing interaction thus minimizing finite-size effects, while also minimizing the finite-bandwidth effect.

The calculations were performed using the density matrix renormalization group method. The conserved quantum numbers are the total number of electrons n and the z -component of total spin S_z . The calculations do not provide differential conductance of the system, but rather the energies of the ground state and a few lowest-lying excitations in each (n, S_z) sector. We index these with an additional quantum number $i = 0, 1, \dots$, $i = 0$ being the ground state of a given sector.

The doublet \rightarrow singlet excitation energy shown in Fig. 2 is thus given by the energy difference between the ground states of the relevant singlet and doublet sectors $\delta E = E(n = 204, S_z = 0, i = 0) - E(n = 203, S_z = 1/2, i = 0)$.

Single-level approximation. The end-to-end spin correlations shown in Fig. 1b were obtained using the zero-bandwidth limit of (1), i.e. by only considering a single level in each SI. This approach allows us to consider a longer chain of alternating SIs and QDs coupled in series and gives qualitatively correct results. The eigenstates and spin correlations were obtained by direct diagonalization in sectors of (n, S_z) .

- * juan.saldana@nbi.ku.dk
- ¹ G. Semeghini, H. Levine, A. Keesling, S. Ebadi, T. T. Wang, D. Bluvstein, R. Verresen, H. Pichler, M. Kalinowski, R. Samajdar, A. Omran, S. Sachdev, A. Vishwanath, M. Greiner, V. Vuletić, and M. D. Lukin, “Probing topological spin liquids on a programmable quantum simulator,” *Science* **374**, 1242–1247 (2021).
 - ² L. Hofstetter, S. Csonka, J. Nygård, and C. Schönberger, “Cooper pair splitter realized in a two-quantum-dot Y-junction - Nature,” *Nature* **461**, 960–963 (2009).
 - ³ Antti Ranni, Fredrik Brange, Elsa T. Mannila, Christian Flindt, and Ville F. Maisi, “Real-time observation of Cooper pair splitting showing strong non-local correlations - Nature Communications,” *Nat. Commun.* **12**, 1–6 (2021).
 - ⁴ Juan Carlos Estrada Saldaña, Alexandros Vekris, Luka Pavešič, Peter Krogstrup, Rok Žitko, Kasper Grove-Rasmussen, and Jesper Nygård, “Excitations in a superconducting Coulombic energy gap,” arXiv (2021), 2101.10794.
 - ⁵ Eduardo J. H. Lee, Xiaocheng Jiang, Manuel Houzet, Ramón Aguado, Charles M. Lieber, and Silvano De Franceschi, “Spin-resolved Andreev levels and parity crossings in hybrid superconductor–semiconductor nanostructures,” *Nat. Nanotechnol.* **9**, 79–84 (2013).
 - ⁶ T. Hensgens, T. Fujita, L. Janssen, Xiao Li, C. J. Van Diepen, C. Reichl, W. Wegscheider, S. Das Sarma, and L. M. K. Vandersypen, “Quantum simulation of a Fermi–Hubbard model using a semiconductor quantum dot array - Nature,” *Nature* **548**, 70–73 (2017).
 - ⁷ Luka Pavešič and Rok Žitko, “Qubit based on spin-singlet Yu-Shiba-Rusinov states,” *Phys. Rev. B* **105**, 075129 (2022).
 - ⁸ Luka Pavešič, Daniel Bauernfeind, and Rok Žitko, “Yu-Shiba-Rusinov states in superconducting islands with finite charging energy,” arXiv:2101.10168 (2021), 2101.10168.
 - ⁹ Stevan Nadj-Perge, Ilya K. Drozdov, Jian Li, Hua Chen, Sangjun Jeon, Jungpil Seo, Allan H. MacDonald, B. Andrei Bernevig, and Ali Yazdani, “Observation of majorana fermions in ferromagnetic atomic chains on a superconductor,” *Science* **346**, 602–607 (2014).
 - ¹⁰ L. Campos Venuti, C. Degli Esposti Boschi, and M. Roncaglia, “Long-Distance Entanglement in Spin Systems,” *Phys. Rev. Lett.* **96**, 247206 (2006).
 - ¹¹ D. L. Cox and M. Jarrell, “The two-channel Kondo route to non-Fermi-liquid metals,” *J. Phys.: Condens. Matter* **8**, 9825–9853 (1996).
 - ¹² A. J. Heeger, S. Kivelson, J. R. Schrieffer, and W.-P. Su, “Solitons in conducting polymers,” *Rev. Mod. Phys.* **60**, 781–850 (1988).
 - ¹³ S. Doniach, “The Kondo lattice and weak antiferromagnetism,” *Physica B+C* **91**, 231–234 (1977).
 - ¹⁴ Daria V. Beznasyuk, Sara Martí-Sánchez, Jung-Hyun Kang, Rawa Tanta, Mohana Rajpalke, Tomaš Stankevič, Anna Wulff Christensen, Maria Chiara Spadaro, Roberto Bergamaschini, Nikhil N. Maka, Christian Emanuel N. Petersen, Damon J. Carrad, Thomas Sand Jespersen, Jordi Arbiol, and Peter Krogstrup, “Doubling the mobility of InAs/InGaAs selective area grown nanowires,” arXiv (2021), 2103.15971.
 - ¹⁵ Shawulienu Kezilebieke, Marc Dvorak, Teemu Ojanen, and Peter Liljeroth, “Coupled Yu–Shiba–Rusinov States in Molecular Dimers on NbSe₂,” *Nano Lett.* **18**, 2311–2315 (2018).

ACKNOWLEDGEMENTS

We thank Felix Von Oppen, Ramon Aguado, Martin Zonda and Andras Palyi for useful discussions. Additionally, we thank Peter Krogstrup for providing the nanowire materials.

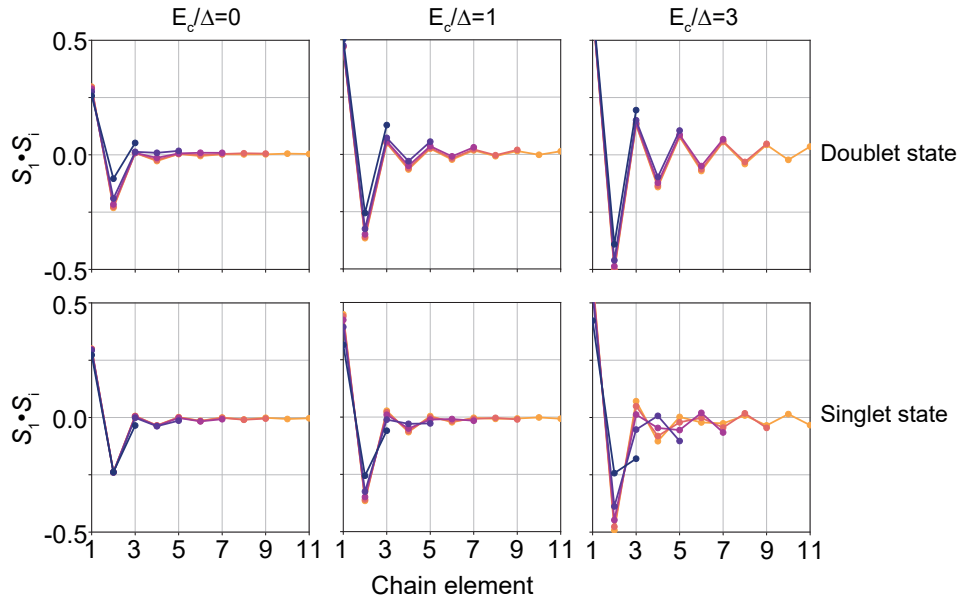
Funding: The project received funding from the European Union’s Horizon 2020 research and innovation program under the Marie Skłodowska-Curie grant agreement No. 832645. We additionally acknowledge financial support from the SolidQ project by the Novo Nordisk foundation, Carlsberg Foundation, the Independent Research Fund Denmark, QuantERA ‘SuperTop’ (NN 127900), the Danish National Research Foundation, Villum Foundation project No. 25310, and the Sino-Danish Center. L. P. and R. Ž. acknowledge the support from the Slovenian Research Agency (ARRS) under Grant No. P1-0044, P1-0416, and J1-3008.

AUTHOR CONTRIBUTIONS STATEMENT

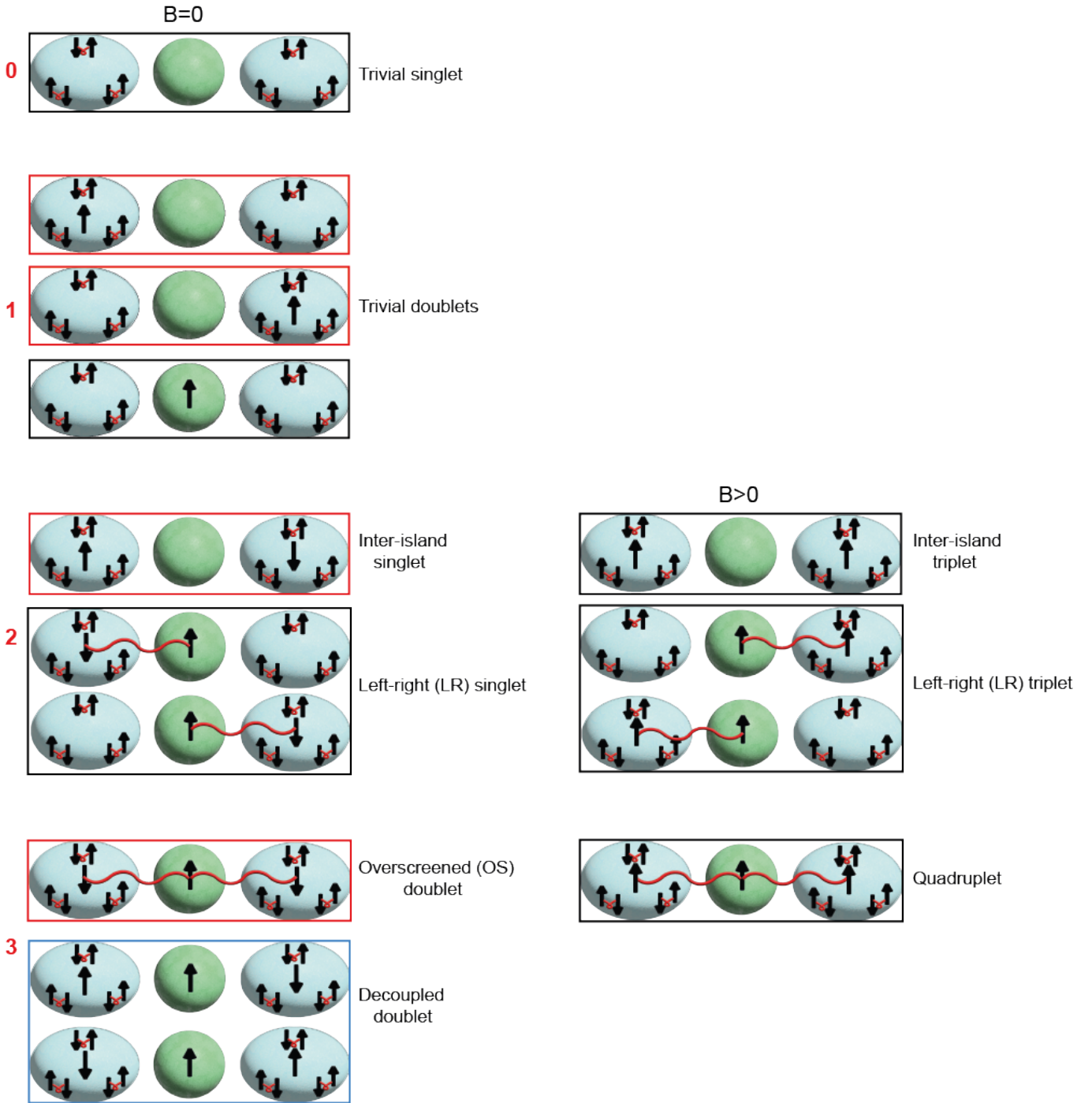
J.C.E.S. conceived the experiments with input from all co-authors. A.V. fabricated the device. J.C.E.S. and A.V. did the experiments. J.C.E.S. performed the data analysis with input from A.V., K.G.R. and J.N. J.C.E.S. L.P. and R.Ž. interpreted the experimental data. L.P. and R.Ž. did the theoretical analysis. J.C.E.S. wrote the manuscript with input from all co-authors.

ADDITIONAL INFORMATION

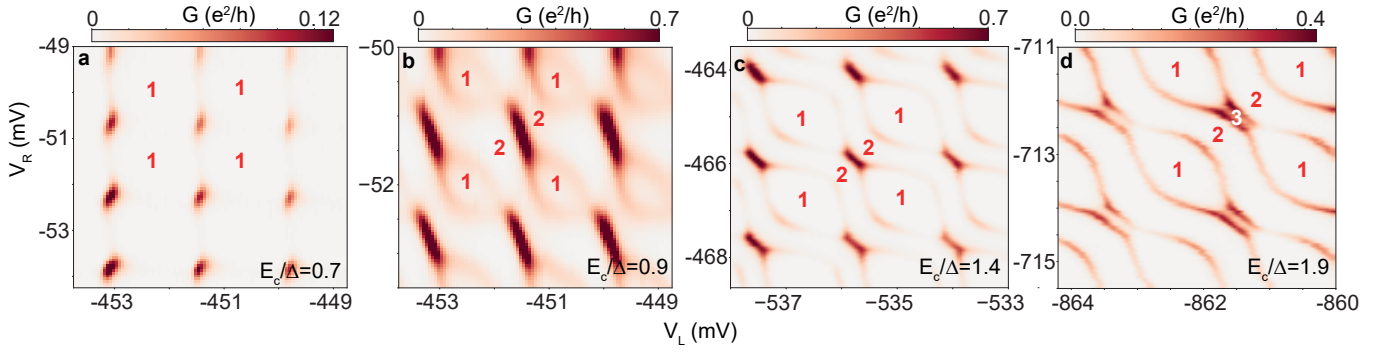
Supplementary Information is available for this paper. The authors declare no competing interests.



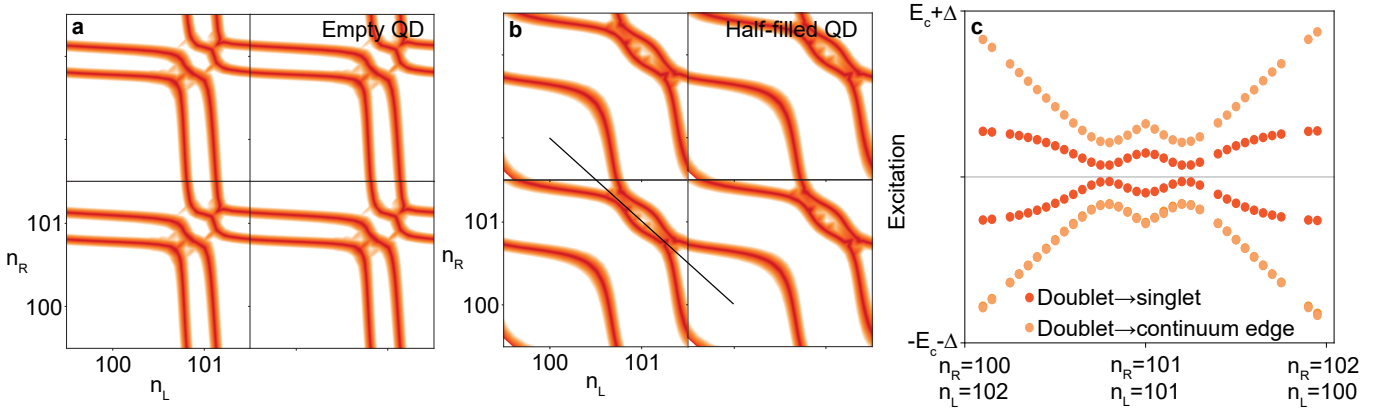
Extended Data Figure 1. **Spin-spin correlations in alternating superconducting island - quantum dot chains.** Correlations between the first spin, S_1 , of the alternating SI-QD chain and the spin in position i , S_i , calculated with the single-level approximation. Each panel contains results for chains of different odd length, 3, 5, 7, 9 and 11. Left, central and right panels correspond to $E_c/\Delta = 0, 1$ and 3. Top panels examine correlations in the doublet state, while bottom ones examine correlations in the singlet state. In the doublet state, the correlations cross zero between adjacent elements for $E_c/\Delta = 1$ and 3, indicating long-range order. The long-range order is lost for $E_c/\Delta = 0$ and for any E_c/Δ value in the singlet state.



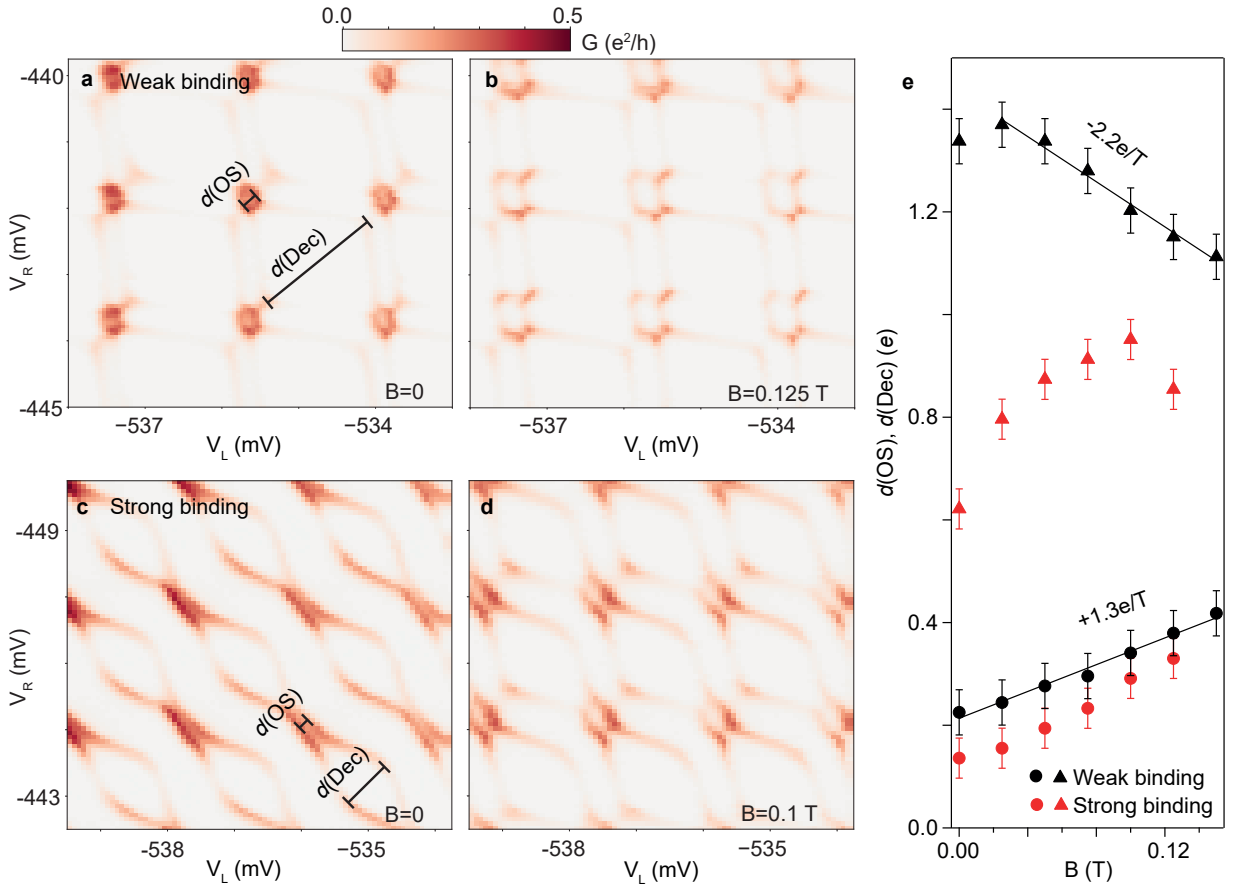
Extended Data Figure 2. **Ground state for different number of local moments.** Depictions of the wavefunction of the ground state of the SI-QD-SI chain for different total number of LMs. Red frames indicate that the state is only the GS for $E_c > \Delta$, while blue frames indicate that the state is only the GS for $E_c < \Delta$. States with black frames can be the GS at any finite E_c . States at the left column can be the GS at $B = 0$, and those at the right column may become the GS only at $B > 0$. The states on the left column may become the GS at $B > 0$ independently of the E_c/Δ ratio.



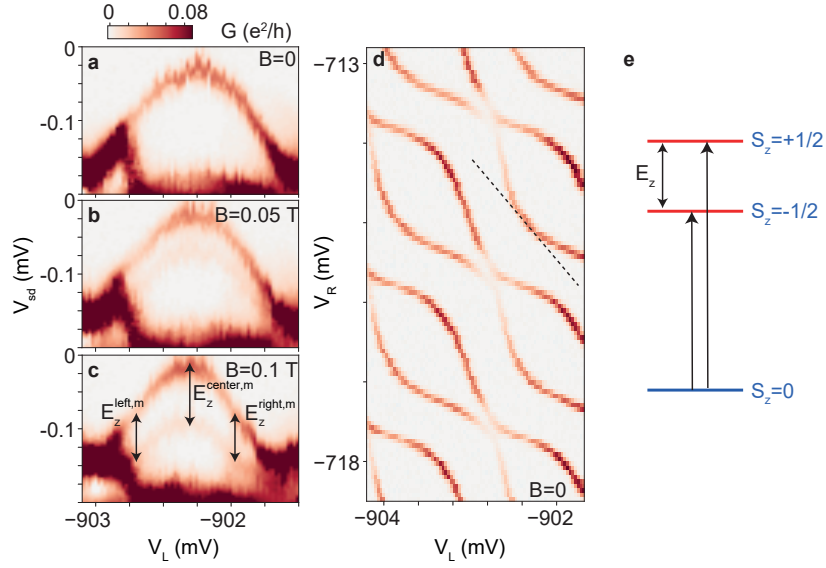
Extended Data Figure 3. **Development of the overscreened doublet with E_c/Δ .** **a-d** Zero-bias G stability diagrams in the strong binding regime versus V_L , V_R for different QD shells and different E_c/Δ . A LM is fixed in the QD. Numbers in the diagram indicate the total number of LMs in the device for different gate regions. **a** The GS is a trivial doublet. The conductance is enhanced due to Andreev reflection when four doublets differing by a Cooper pair in their charge are degenerate. **b** The GS alternates between a trivial doublet (1 LM) and a LR singlet. The strong conductance line (saturated scale) connecting two doublets is due to the degeneracy of two LR singlets differing by a Cooper pair in their total charge. **c** The strong conductance line connecting the trivial doublets shrinks. **d** The line gives place to a 3 LM sector hosting an OS doublet GS.



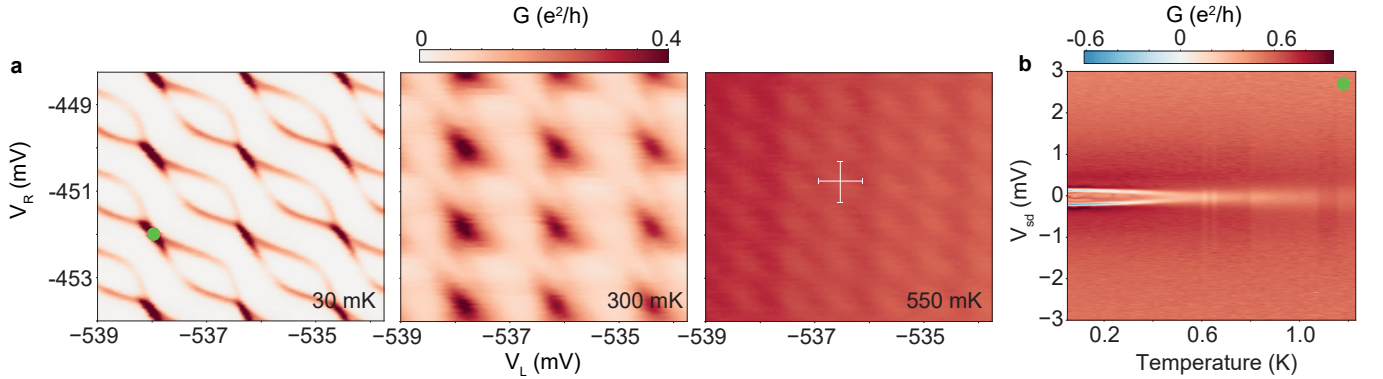
Extended Data Figure 4. **Calculations of the stability diagram and excitations with DMRG.** **a, b** Calculations of the stability diagram for **(a)** an empty and **(b)** half-filled QD versus gate-induced charges in the left and right SIs, n_L and n_R , as done in the experiment in Figs. 2a,b. Lines in the diagrams indicate GS transitions between doublet and singlet states. **c** Calculation of the excitation energy with n_L , n_R swept along the diagonal line in **(b)** as in the experiment in Figs. 3a,b and 4a,c. Red dots indicate excitations from the doublet GS to the excited LR singlet, while yellow dots denote excitations to the edge of the singlet continuum. $U/\Delta = 3.9$, $E_c/\Delta = 1.5$, $\Gamma/U = 0.2$ and $V/U = 0.1$, where V is the interdot charging energy between the QD and each SI. The calculations are in qualitative agreement with the experimental data.



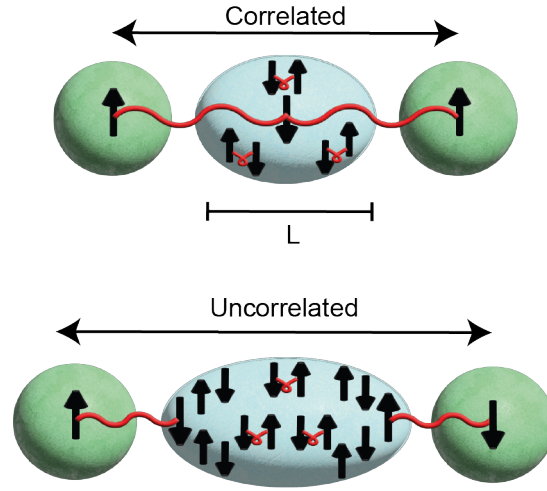
Extended Data Figure 5. **Evolution of the stability diagram in a magnetic field.** **a-d** Zero-bias conductance stability diagrams recorded at different B indicated on each plot. The device parameters are identical to those of Fig. 4, i.e. **(a,b)** $E_B/2E_c = 0.04$ (weak binding), $E_c/\Delta = 1.45$ and **(c,d)** $E_B/2E_c = 0.32$ (strong binding), $E_c/\Delta = 1.65$. **e** B dependence of the diagonal sizes in the 3 LM (circles) and 1 LM (triangles) sectors extracted from stability diagrams for weak (black symbols) and strong binding (red symbols). The sizes at $B = 0$ are given by the bars in **(a)**, **(b)**. Lines are fits to the weak-binding data, with slopes indicated above each line. The data is qualitatively consistent with the Zeeman shifts of the excitation energies shown in Fig. 4e.



Extended Data Figure 6. **Zeeman splitting of left-right singlet to doublet excitations.** **a-c** Magnetic field, B , dependence of the G versus source-drain bias, V_{sd} , with the gates V_L and V_R swept along the dashed line in the zero-bias G stability diagram in **(d)**. For simplicity, only V_L is indicated. The QD is half-filled, left-right binding energies are approximately symmetric and strong ($E_B/2E_c = 0.15 > \mathcal{E}$), and $E_{cL}/\Delta_L \approx E_{cR}/\Delta_R = 1.9$. The curved line in the measurement represents singlet \rightarrow doublet excitations with gate-dependent state mixing, with the doublet state splitting into spin-up and spin-down components as B is increased. In **(c)**, Zeeman energies at three spots in the split curve are indicated by double-headed arrows; they highlight that the splitting is larger at the center of the curve. The colorscale is saturated to highlight the faint excitations. The g factors of the three device components are fairly symmetric: $g_L = 12.6$, $g_N = 15$ and $g_R = 11$. The Zeeman splitting at the center is $E_z^{\text{center,m}} = 85 \pm 18 \mu\text{eV}$, which matches well the Zeeman splitting of the trivial doublet excitation $E_z^{\text{center}} = g_N \mu_B B = 87 \mu\text{eV}$ as expected. At the left and right sides, the Zeeman splitting is $E_z^{\text{left,m}} = E_z^{\text{right,m}} = 67 \pm 16 \mu\text{eV}$. The expected Zeeman splittings three-quarters of the way (in gate voltage) to the OS doublet are $E_z^{\text{left}} = E_z^{\text{right}} = 0.5g_N \mu_B B + 0.5(n_L g_L + n_R g_R) \mu_B B$, where n_L and n_R are the gate-induced charges in the left and right SIs. These evaluate as $E_z^{\text{left}} = 54 \mu\text{eV}$ for $n_L = 0.75$, $n_R = 0.25$, and $E_z^{\text{right}} = 68 \mu\text{eV}$ for $n_L = 0.25$, $n_R = 0.75$, matching within error bars the measurements. **e** Schematics of singlet \rightarrow doublet excitations (arrows). The energy difference between the excitations provides a measure of the Zeeman energy.



Extended Data Figure 7. **Temperature dependence.** **a** Zero-bias G stability diagrams recorded at different temperature indicated on each plot in the strong binding regime. The temperature broadens the features, progressively destroys Coulombic and superconducting components of the energy gap, and eventually leads to $1e$ -periodic Coulomb resonances (separated by bars in the diagram at 550 mK) when the superconducting gap becomes populated with quasiparticles. Coulomb blockade is lost in the left island at 900-1200 mK and in the right island at 900 mK. **b** Temperature dependence of the bias spectrum with gates V_L , V_R set at the middle of the OS GS sector (green dot in **a**). We relate the white features at low bias with the closure of the superconducting gap. The superconducting gap closes at ≈ 600 mK independently of the occupation of the islands. The dip at zero bias above 600 mK is modulated by the island gates up to at least 900 mK and it is thus related to Coulomb blockade.



Extended Data Figure 8. **Cleavage of the Yu-Shiba-Rusinov screening cloud in an inverted chain.** Two schematics of the possible fate of the quasiparticle screening cloud for a QD-SI-QD chain with a SI of length L and a E_c/Δ ratio. The top panel is the ideal case required for long-range triplet correlations in a longer alternating SI-QD chain. We speculate that, at certain long enough L and/or small enough E_c/Δ values, separate quasiparticle screening clouds (arrows on the sides of the SI) will form for each QD spin, as seen in the $E_c = 0$ case in well-separated magnetic dimers on superconducting substrates¹⁵. This destroys the long-range correlations of the longer chain in Fig. 1 by changing the GS of the short QD-SI-QD chain into a singlet.